


## Stress Formation During In-Ga Interdiffusion in Thin-Film $\text{CuIn}_{1-x}\text{Ga}_x\text{Se}_2$ Absorber Layers Leads to Stable Ga Gradients

Stefan Schäfer<sup>✉,\*</sup>, Helena Stange, José A. Márquez, Christoph Genzel, and Roland Mainz<sup>✉,†</sup>  
*Helmholtz-Zentrum Berlin für Materialien und Energie GmbH, Hahn-Meitner Platz 1, Berlin 14109, Germany*

 (Received 24 February 2020; revised 19 June 2020; accepted 29 July 2020; published 21 August 2020)

To optimize the opto-electronic properties of compound semiconductors, a detailed understanding and control of compositional gradients forming during their synthesis is crucial. A common fabrication process for  $\text{Cu}(\text{In}, \text{Ga})\text{Se}_2$  (CIGS) thin-film solar cells uses annealing at high temperatures, which—contrary to what could be expected from simple Fickian diffusion—results in the formation of steep and stable Ga gradients, deviating from the optimal Ga profile for high-efficiency CIGS absorbers. Here, we show that the formation of elastic stresses inside the material during the interdiffusion can have a profound effect on the final Ga distribution, resulting in persistent Ga gradients inside CIGS absorber layers. A comparison of numerical diffusion and stress-formation calculations with real-time synchrotron-based energy-dispersive x-ray diffraction data acquired in-situ during selenization of CIGS thin films demonstrates that the model can reproduce the stagnation of In-Ga interdiffusion. We discuss that a detailed understanding of the interplay between stress and diffusion processes in thin films may open alternative fabrication strategies for generating desired stable compositional gradients to improve the opto-electronic properties of compound semiconductors, such as chalcopyrite, kesterite, and perovskite solar cell absorbers for solar cells.

DOI: [10.1103/PhysRevApplied.14.024063](https://doi.org/10.1103/PhysRevApplied.14.024063)

### I. INTRODUCTION

Compound semiconductors containing isovalent atomic pairs are among the most interesting materials for thin-film solar cell absorbers [1–4]. Their bandgap can usually be affected by the formation of compositional gradients during synthesis. For  $\text{Cu}(\text{In}, \text{Ga})\text{Se}_2$  (CIGS) thin-film solar cells, the out-plane Ga gradient—more specifically, the  $[\text{Ga}]/([\text{Ga}]+[\text{In}])$  ratio (GGI ratio)—over the absorber layer is one of the key features determining the device efficiency, requiring careful tuning to achieve optimal device parameters [5–8]. A widely used production method for CIGS solar cells is sequential processing, which comprises the annealing of a metallic precursor in a Se-containing atmosphere [9]. Devices manufactured in the sequential fabrication process usually exhibit a strong and stable GGI gradient increasing towards the back contact [8]. This gradient forms during the selenization due to increased In diffusivity, which leads to In migration towards the absorber's front, while the Ga remains at the absorber's back contact. This segregation often results in two almost pure phases after the selenization: a Ga-rich phase (roughly  $\text{CuGaSe}_2$ ) at the back contact and an In-rich phase (roughly  $\text{CuInSe}_2$ ) near the surface [10–12]. Although a moderate GGI increase towards the back of the thin film can have beneficial effects due to reduced recombination losses, low

Ga concentrations in the front and middle part of the layer will lead to below optimum bandgap values and thus to reduced conversion efficiencies [7].

In and Ga share the same lattice sites in the CIGS lattice; therefore, they can be expected to interdiffuse in the presence of intrinsic concentration gradients, as found after the selenization of the film. In-Ga interdiffusion is indeed observed during and after the selenization phase in the sequential fabrication process [10,13,14]. At low temperatures In-Ga segregation would be expected in equilibrium due to a positive In-Ga mixing enthalpy [15]. However, at typical CIGS fabrication temperatures between 500 and 600 °C the mixing entropy overcompensates the positive mixing enthalpy and hence a complete homogenization of the In and Ga distribution by interdiffusion can be expected. Interestingly, it is found that a strong GGI gradient remains [8] and a detailed understanding of the reasons for the persistence of the gradient is essential for opening adjustment strategies of this crucial device parameter.

In most descriptions of the diffusion process in CIGS a standard Fickian diffusion is assumed to take place [13,16,17]. This means that, in terms of the Gibbs free energy, the only driving force for the diffusion process is changes in the entropy. However, the persistence of a GGI gradient is inconsistent with this explanation. It is a well-established fact that besides mixing entropy and enthalpy, stresses can have a profound effect on diffusion processes [18–20].

\*stefan.schaefer@helmholtz-berlin.de

†roland.mainz@helmholtz-berlin.de

In this work we model In-Ga interdiffusion taking into account the elastic work that has to be performed on the lattice as well as the changes in enthalpy due to the breaking and building of atomic bonds. In CIGS, in-plane stresses can be expected to form during In-Ga interdiffusion due to differing effective radii of Ga and In inside the lattice in combination with the rigidity of the much thicker soda-lime glass substrate. By modeling the effect of stress formation on the In-Ga interdiffusion and comparing them with synchrotron-based real-time energy-dispersive x-ray diffraction (EDXRD) during CIGS synthesis we show that those stresses are not negligible and may be suitable candidates in explaining the persistence of the observed Ga gradients in CIGS. To obtain theoretical predictions of the encompassing effects, we developed an interdiffusion model using the thermodynamics of elastically stressed crystals. Using density functional theory calculations of the enthalpy of mixing in CIGS systems and measured values for different material properties from the literature, we show that our model predicts a stagnation of the interdiffusion process.

Understanding the exact interplay between stress formation and interdiffusion in thin films may reveal alternative possibilities to design deposition procedures that can help control compositional material gradients. Application for such an understanding is not limited to Ga-In interdiffusion in CIGS solar cells, but also has potential applications in Se-S interdiffusion in  $\text{Cu}(\text{In}, \text{Ga})(\text{S}, \text{Se})_2$  (CIGSSe) [21,22], in kesterites,  $\text{Cu}_2\text{ZnSn}(\text{S}, \text{Se})_4$  (CZTSSe) [23–25], and in other light absorbing structures, e.g., perovskites [26,27].

## II. STRESS-HAMPERED INTERDIFFUSION

A CIGS film with a steep Ga gradient, as typically found shortly after selenization of In-Ga-Se precursor films [10,11], is schematically shown in Fig. 1(a), with the corresponding GGI gradient shown in Fig. 1(b) and without in-plane stress [Fig. 1(c)]. The In and Ga concentration gradients impose a driving force for In-Ga interdiffusion, which leads to a decrease of the gradient during further annealing [Figs. 1(d) and 1(e)]. During the diffusion process, differently sized In and Ga ions interchange places and hence expand or contract the local lattice. Because in-plane expansions and contractions of the thin film are inhibited by the much thicker SLG substrate, stress forms: compressive stress forms at the bottom part of the film, where bigger In ions replace smaller Ga ions in the crystal structure, whereas tensile stress forms at the upper part, where smaller Ga ions replace bigger In ions [Fig. 1(f)]. To build up stress inside the system, the diffusion couple has to perform elastic work. This elastic work leads to a reduction of the diffusion potential gradient—the driving force behind the interdiffusion process—and hence hampers In-Ga interdiffusion.

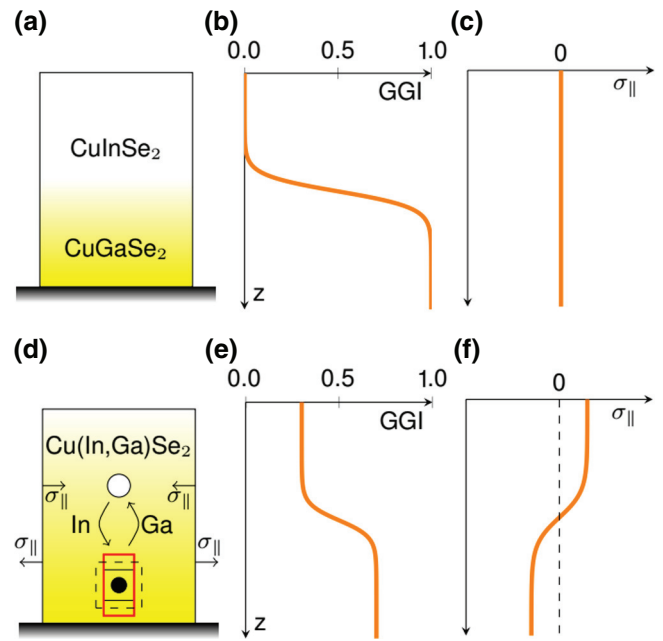


FIG. 1. Schematic drawing of a CIGS film together with the Ga distribution  $x$  (GGI) and in-plane stress distributions over the layer depth. The situations at the onset of interdiffusion and at the end are depicted in the images in the upper [(a)–(c)] and lower [(d)–(f)] rows, respectively.

In the following, we determine the elastic stress depending on the initial and resulting composition distribution and derive the resulting diffusion equation that takes formation of stress into account.

### A. Stress formation

In Fig. 1(b) we schematically show the initial state of the GGI distribution  $x$  as a function of film depth  $z$  at the onset of the interdiffusion,  $x(t=0, z) = x_0(z)$ , and in Fig. 1(e) we show a more intermixed state at some later time  $t$ ,  $x(t, z)$ . Consider a volume of  $\text{Cu}(\text{In}, \text{Ga})\text{Se}_2$  where a Ga ion [filled circle in Fig. 1(d)] is replaced by an In ion (open circle). If the initial volume (solid line square) is not constrained, it would expand to a larger size (dashed line square), with an edge length  $d^r(x)$  (where  $r$  indicates the nonconstrained, relaxed state). However, since the film is attached to a rigid substrate, the size of the volume in the in-plane direction is constrained to its original in-plane extension  $d^r(x_0)$  [red line rectangle in Fig. 1(d)], resulting in an out-plane strain deforming the volume.

The role of the substrate for the formation of stress inside the thin film can also be understood from Fig. 2 [28]. In Fig. 2(a) we depict two thin layers of equal in-plane dimensions consisting of pure CIS and CGS, respectively, as present at the onset of interdiffusion. If the two layers are not attached to each other, the exchange of Ga and In (depicted by filled spheres) would lead to an expansion of the lower layer and a contraction of the upper, as seen

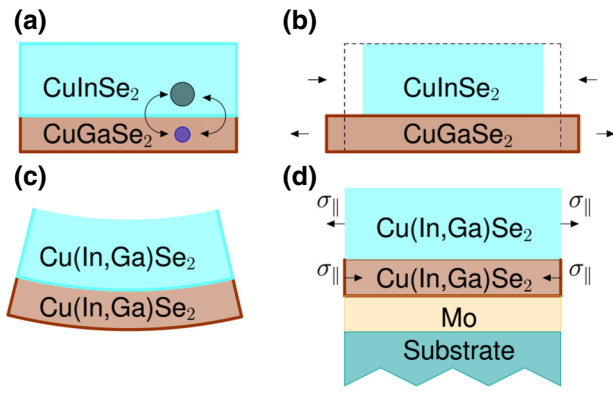


FIG. 2. (a)–(d) Schematic drawing of stress formation in thin films. See the text for details.

in Fig. 2(b). If the layers stay attached to each other, the expansion and contraction will lead to a concave bending of the thin film, as seen in Fig. 2(c). However, the thin film is not free to bend but rigidly attached to a thick SLG/Mo substrate (approximately 3 mm), which is three orders of magnitude thicker than the thin film (approximately  $2 \mu\text{m}$ ). The rigidity of the substrate results in forces acting throughout the thin film, inhibiting bending of the thin film and resulting in tensile and compressive stresses [Fig. 2(d)]. The total system consisting of thin film and substrate might still be subject to bending according to Stoney [29,30]. However, the curvature of bending is proportional to the ratio of the thin film and substrate thicknesses and is thus negligible. This is in accordance with our observation that no bending of the sample is visible.

We note that the influence of the  $1 \mu\text{m}$  thick Mo layer between the glass substrate and the CIGS film on the residual stress in the CIGS film is negligible, since for a system consisting of multiple stacked thin films rigidly attached to a thick substrate, it can be shown that the stress developing in each film solely depends on the imposed misfit strain between this film and the substrate [31–34].

Correspondingly, we define the in-plane elastic strain on a given sublayer of the thin film at position  $z$  by the local change in unit-cell dimensions:

$$\epsilon_{\parallel}[x(z)] = \frac{d^r[x(z)] - d^r[x_0(z)]}{d^r[x(z)]}. \quad (1)$$

Because the film is composed of many differently oriented crystallites, we assume that on average the material is isotropic and that  $d^r(x)$  is proportional to  $\sqrt[3]{V_{\text{UC}}(x)}$ , where  $V_{\text{UC}}(x)$  is the unit cell volume as a function of composition  $x$  (see Sec. IID for details).

The stress state of the film can then be described by two independent components, the in-plane stress  $\sigma_{\parallel} = \sigma_{xx} = \sigma_{yy}$  and the out-plane stress  $\sigma_{\perp} = \sigma_{zz}$ . The resulting in-plane stresses are given by Hook's law that, for a thin film,

takes the form [32,35]

$$\sigma_{\parallel}[x(z)] = \frac{Y}{1-\nu} \epsilon_{\parallel}[x(z)]. \quad (2)$$

Here,  $Y$  is Young's modulus and  $\nu$  is the Poisson ratio of the material. Because the film is not constrained in the out-plane direction, the out-plane stress vanishes [35]:  $\sigma_{\perp} = 0$ .

An in-plane stress acting on a thin film will, following Poisson's relation, result in out-plane strains,  $\epsilon_{\perp}(\sigma_{\parallel})$ . Hook's law for  $\sigma_{\perp}$  together with  $\sigma_{\perp} = 0$  relates the out-plane strain to the in-plane stresses,

$$\epsilon_{\perp} = \frac{-2\nu}{Y} \sigma_{\parallel}. \quad (3)$$

## B. The diffusion equation

To consider the effect of stress on the interdiffusion, we need to express the diffusion equation in terms of a generalized diffusion potential. Fick's second law connects the change in time of the Ga density,  $\rho_G$ , inside a given volume of our system to the inflow and outflow into and from this volume. Denoting the net Ga flux by  $J$ , assuming lateral homogeneity and a compositional gradient in the out-plane  $z$  direction, this can be written as

$$\frac{\partial \rho_G}{\partial t} = -\frac{\partial J}{\partial z}. \quad (4)$$

Since Ga and In are assumed to be the only diffusing species, their net flux must vanish and the In flux must be of equal size and opposite direction than  $J$ . In order for that to be possible, the tracer-diffusion coefficients of In,  $D_I^*$ , and Ga,  $D_G^*$ , have to be equal:  $D^* := D_I^* = D_G^*$  [36]. While Cu vacancies provide the primary diffusion path for In and Ga in CIGS [37] and therefore influence the magnitude of the diffusion coefficient, they are present only in negligible numbers relative to In and Ga and can thus be neglected as an independent diffusing species in a first approximation. See Sec. IID for details.

The Ga flux can be expressed by generalized thermodynamic forces or by the spatial gradients of the corresponding potentials [38]. The potential in the case of diffusion in a crystal is called the diffusion potential, denoted by  $M$  [39], and describes the energy change when interchanging an In for a Ga atom. In a system comprised of a diffusion couple with negligible vacancy concentration, Onsager's relations dictate the functional dependence between  $J$  and  $M$  [40],

$$J = -L \frac{\partial M}{\partial z}, \quad (5)$$

where  $L$  is the phenomenological coefficient of the system.

Using diffusion kinetics in crystals, it can be shown that the flux is connected to the intrinsic diffusion coefficient,  $D^I$ , and the tracer-diffusion coefficient,  $D^*$ , by [36]

$$J = -D^I \frac{\partial \rho_G}{\partial z} = -D^* \alpha(x) \rho \frac{\partial x}{\partial z}. \quad (6)$$

Here  $\rho$  is the combined density of In and Ga inside the material such that  $\rho_G = x\rho$ . Furthermore,  $\rho$  is calculated with respect to a constant reference volume and is thus also constant (see Sec. II D). The effect of driving forces other than the concentration gradient on the interdiffusion is incorporated into the thermodynamic factor,  $\alpha$ . Expressing  $M$  as a function of  $x(z)$  allows us to reformulate Eq. (5) in terms of a spatial gradient of composition  $x$ , equating the result with Eq. (6) to obtain the phenomenological coefficient

$$L = \frac{D^*}{kT} x(1-x)\rho. \quad (7)$$

(See Appendix D for a more detailed derivation.) The diffusion equation (4) can then be written as

$$\frac{\partial x}{\partial t} = \nabla_z \left\{ \frac{D^*}{kT} x(z)[1-x(z)] \nabla_z M[x(z)] \right\}. \quad (8)$$

The effect of stress formation on interdiffusion can be incorporated into the dependence of the diffusion potential on  $x$ , as derived in the next section.

### C. Diffusion potential

Finally, we need to find an analytical expression for the diffusion potential  $M$  in Eq. (8) to determine the influence of stress on the interdiffusion. Diffusion is driven by the minimization of the Gibbs free energy of the total system. The total differential of the Gibbs free energy density,  $g$ , for a binary, crystalline system under nonhomogeneous stress can be written in the form [39]

$$dg = -sdT - \epsilon_{ij} d\sigma_{ij} + M \rho dx. \quad (9)$$

Here,  $s$  is the entropy density,  $\epsilon$  and  $\sigma$  are the elastic strain and stress, and  $T$  is the temperature. In terms of the chemical potentials of the single species,  $\mu_i$ ,  $i \in [\text{In}, \text{Ga}]$ ,  $M$  is given by

$$M = \mu_{\text{Ga}} - \mu_{\text{In}}. \quad (10)$$

Because we work in an isothermal environment we set  $dT = 0$  in Eq. (9). Integrating the appropriate Maxwell relation for Eq. (9) from the stress-free state to the actual state then allows us to derive an equation for  $M$ ,

$$M(x, Y, \nu) = M^0(x) + \frac{2}{\rho} \frac{\partial \epsilon_{\parallel}(x)}{\partial x} \sigma_{\parallel}(x, Y, \nu) \quad (11)$$

with the in-plane strain  $\epsilon_{\parallel}$  and stress  $\sigma_{\parallel}$  from Eqs. (1) and (2), where the composition  $x = x(z)$  is a function of film

depth  $z$ . Note that the strain and stress also depend on the initial composition  $x_0$  and that  $M^0$  is the diffusion potential in the stress-free state,  $\sigma_{ij} = 0$ , which according to Eq. (9) is

$$M^0(x) = \frac{1}{\rho} \frac{\partial g^0(x)}{\partial x}. \quad (12)$$

Here  $g^0$  is the Gibbs free energy density for a system not subject to any stresses and strains:

$$g^0 = -Ts + h \quad (13)$$

with  $h$  the enthalpy density. [See Appendix C for more details on the derivation of Eq. (11) and Sec. II E for the exact functional form of  $g^0$ .]

### D. Further modeling assumptions

In and Ga occupy the same lattice sites in the tetragonal crystal structure of CIGS and the number of those lattice sites is  $N^{\text{UC}} = 4$  per unit cell.

The total number of lattice sites  $N_0$  is assumed to stay constant throughout the interdiffusion since no phase transitions occur and so the crystal structure, especially the Se and Cu sublattices, stays unaltered. Furthermore, all lattice sites of the In-Ga sublattice are to be occupied by either Ga or In atoms, which leads to

$$N_0 = N_G + N_I, \quad (14)$$

$$\Rightarrow dx = -dx_I, \quad (15)$$

where  $N_G$  and  $N_I$  are the numbers of Ga and In atoms in the absorber, respectively, and  $x_I = 1 - x$  is the ratio  $[\text{In}]/([\text{Ga}]+[\text{In}])$ .

Relation (15) holds for the sample as a whole as well as for the GGI in a single sublayer and states that only In and Ga take part in the diffusion process. The number of vacancies is considered negligible in comparison to the number of host atoms and they are considered to be in thermal equilibrium throughout the process, maintained by constant creation and destruction at the surface of the thin film and at dislocations and point defects [41].

The influence of Cu vacancies on the elastic properties can be estimated by positron-annihilation experiments measuring the density of Cu mono- and divacancies [42] in CIGS. These measurements report densities of around  $0.5 \times 10^{18}$  per cubic centimeter at room temperature. We can then estimate the Cu vacancy fraction at the process temperature of 600°C by calculating the vacancy formation enthalpy from the reported measurements [41]. This results in a Cu vacancy fraction of approximately 0.02 at process temperature that may, to a good approximation,



be neglected in determining the stress state of the material. Furthermore, since the Cu vacancies are the dominant diffusion path of Ga and In in CIGS [37], their diffusion coefficient will be proportional to the defect density. The diffusion coefficient in turn influences the time scale of the problem but not, as shown in Appendix E, the steady-state Ga distribution, which depends on the diffusion potential and thus on the elastic parameters of the problem.

The stress-free, or relaxed, state of the material is defined as the state in which every unit cell is allowed to expand and contract freely according to its GGI. In this state we suppose that the lattice parameters follow Vegard's law [43], i.e., the dependence of the lattice parameters on the GGI,  $x$ , reads

$$a^0(x) = a_G x + (1 - x)a_I, \quad (16)$$

$$c^0(x) = c_G x + (1 - x)c_I, \quad (17)$$

where  $a_G$ ,  $c_G$  and  $a_I$ ,  $c_I$  denote the lattice parameters for pure CGS and CIS, respectively, and  $a^0$  and  $c^0$  denote the resulting lattice parameters at room temperature,  $T_0$ . Because the annealing and the measurement are performed at an ambient temperature of  $T = 600^\circ\text{C}$  we have to take into account the thermal expansion of the material. The resulting lattice parameters in the stress-free state,  $a$  and  $c$ , at temperature  $T$  can be calculated using

$$a(x) = a^0(x)[1 + \alpha_a(x)\Delta T], \quad (18)$$

$$c(x) = c^0(x)[1 + \alpha_c(x)\Delta T]. \quad (19)$$

Here,  $\alpha_a(x)$  and  $\alpha_c(x)$  denote the coefficients of thermal expansion (CTE) for the lattice parameters  $a$  and  $c$ , respectively, at a given GGI of  $x$  and  $\Delta T = T - T_0$ . We assume that the CTEs follow a linear dependence on  $x$  in the range of interest and define alloyed CTEs by

$$\alpha_a(x) = \alpha_a^{\text{CGS}} x + (1 - x)\alpha_a^{\text{CIS}}, \quad (20)$$

$$\alpha_c(x) = \alpha_c^{\text{CGS}} x + (1 - x)\alpha_c^{\text{CIS}}. \quad (21)$$

The coefficients  $\alpha_{a/c}^{\text{CGS/CIS}}$  denote the CTEs for the  $a$  and  $c$  lattice parameters for CIS and CGS, respectively, and are given in Table I.

Since we do not take into account neither the microstructure of the thin film nor the exact unit-cell alignments over an entire layer, we use an effective in-plane lattice parameter,  $a_{\parallel}$ , as indicator for the in-plane strains. We define this

lattice parameter as

$$a_{\parallel}(x) := \sqrt[3]{V_{\text{UC}}[a(x), c(x)]} = \sqrt[3]{a(x)^2 c(x)}, \quad (22)$$

where  $V_{\text{UC}}$  is the unit-cell volume. We use  $a_{\parallel}$  to calculate the elastic strain in a layer of given composition from Eq. (1), so  $a_{\parallel} \equiv d'$ .

Finally, we do not consider initial stresses to be present in the absorber, assuming that, during the phase transitions of the selenization process, any initial stress field is sufficiently reduced.

### E. Numerical modeling of interdiffusion with stress formation

To predict the effect of stress on the In-Ga interdiffusion in a CIGS film with an initial composition gradient as depicted in Fig. 1(a), we solved the diffusion equation (8) with the diffusion potential given by Eq. (11) numerically using an explicit finite difference discretization scheme. To this end, we split the system depicted in Fig. 1(a) into  $N_L$  equally sized layers of thickness  $d_0 = d/N_L$  and calculated for each the diffusion potential and corresponding fluxes according to Eqs. (11) and (5) and their spatial derivatives by means of central differences. The spatial flux derivatives then allow for the solution of the explicitly discretized version of the diffusion equation.

The input parameters for the modeling are taken from the literature and are given in Table I. Note that the literature values for the diffusion coefficient  $D^*$  for In-Ga interdiffusion in CIGS vary widely, from  $10^{-11}$  to  $10^{-14}$   $\text{cm}^2/\text{s}$  [13,16,17,49,50]. (Numerical values for diffusion coefficients given here represent the arithmetic means of Ga and In diffusivities determined in the references.)

Xue *et al.* [48] determined  $g^0$  from Eq. (13) using DFT calculations for the intermixing of a CGS and a CIS phase at a specific Ga content  $x$ :

$$g^0(x) = -Ts(x) + h(x), \quad (23)$$

$$s(x) = -k\rho[x \ln x + (1 - x) \ln(1 - x)], \quad (24)$$

$$h(x) = x(1 - x)\rho\Omega(x), \quad (25)$$

$$\Omega(x) = \alpha x^2 + \beta x + \gamma. \quad (26)$$

Here  $s$  and  $h$  are the entropy- and enthalpy density, respectively,  $k$  is the Boltzmann constant, and  $\alpha$ ,  $\beta$ , and  $\gamma$  are phenomenological constants, which are given in Table I.

Generally, Young's modulus  $Y$  will depend on composition, which will give rise to additional terms in the diffusion potential, Eq. (11) (see Appendix C for a detailed derivation). If this dependence is sufficiently small, these additional terms can be neglected. The literature is not unambiguous with regard to the variation of elastic parameters with composition. Reported measurements and

TABLE I. Parameters used for all interdiffusion simulations.

Parameter	Value	Ref.
Lattice parameter $a_G$	0.5614 nm	[44]
Lattice parameter $a_I$	0.5781 nm	[44]
Lattice parameter $c_G$	1.1031 nm	[44]
Lattice parameter $c_I$	1.161 nm	[44]
Poisson ratio $\nu$	0.3	[45]
CTE $\alpha_{\text{CIS}}^a$	$11.4 \times 10^{-6}$ 1/K	[46]
CTE $\alpha_{\text{CIS}}^c$	$8.6 \times 10^{-6}$ 1/K	[46]
CTE $\alpha_{\text{CGS}}^a$	$13.1 \times 10^{-6}$ 1/K	[47]
CTE $\alpha_{\text{CGS}}^c$	$5.2 \times 10^{-6}$ 1/K	[47]
Enthalpy coefficient $\alpha$	0.1261 eV	[48]
Enthalpy coefficient $\beta$	-0.1091 eV	[48]
Enthalpy coefficient $\gamma$	0.1018 eV	[48]
Measured average diffusion coefficients of In and Ga $D$	$(10^{-11} - 10^{-14})$ cm <sup>2</sup> /s	[13,16,17,49,50]
Young's modulus of CIGS $Y$	68.9 GPa	[51]
Process temperature $T$	600 °C	...
Integral GGI of sample $\lambda$	0.27	...
Diffraction angle $2\Theta$	6.08	...

calculations of the elastic coefficients of CIS and CGS imply differences in elastic parameters between 2 and 20 GPa [51–56]. However, as argued in Appendix C, even a difference of 20 GPa may be approximately neglected, as done subsequently. In the following simulation we used a diffusion coefficient of  $D = 8.8 \times 10^{-12}$  cm<sup>2</sup>/s and a Young modulus of  $Y = 68.9$  GPa.

The results of the modeling of In-Ga interdiffusion under the influence of stress formation based on these literature data are shown in Fig. 3. For each quantity, the distribution over the layer depth is shown for different simulation times.

It can be seen in Fig. 3(a) that a significant gradient in the GGI composition prevails if the formation of stress is regarded in the In-Ga interdiffusion process. In Fig. 3(b) we present the depth-dependent stress that forms during the interdiffusion process—leading to compressive stress in the Ga-rich bottom part of the film and tensile stress in the In-rich part. Although after 15 min a composition gradient is still present [blue line in Fig. 3(a)] that on its own would drive further interdiffusion, the contribution by the stress gradient in Fig. 3(b) leads to a flat gradient of the total diffusion potential  $M$  [Fig. 3(c)], resulting in a steady state without further interdiffusion. The diffusion potential comprises the energy released due to changes in the entropy and enthalpy of mixing as well as the change in elastic strain energy.

Note that the shape of the final Ga distribution does not depend on the size of the diffusion coefficient  $D^*$ , which, due to the linearity in  $t$  of the diffusion equation (8), only determines how fast this steady-state distribution is approached. The final form of the Ga distribution, i.e., the step size of the final GGI distribution, is determined by the magnitude of Young's modulus.

We note that plastic deformations are not included in the model. The yield stress for CIGS is reported to be  $\sigma_Y \approx 1.1$  GPa (Ref. [51]) and, from Fig. 3(a), it can be seen that the predicted maximum stress inside the thin film is of the same order of magnitude. If the elastic stress exceeds the yield stress, plastic deformation, e.g., by grain boundary migration or formation of dislocations, would be expected to take place, hence limiting the magnitude of the maximal stress in the sample. In comparison to the simulation shown in Fig. 3, the maximum stress would then be smaller, which—according to Eq. (11)—will lead to a smaller stress-dependent term in the diffusion potential and thus to an increased interdiffusion. Furthermore, the reported elastic parameters, e.g., the yield stress and Young's modulus, are temperature- and composition- dependent quantities. Because we work at an elevated process temperature we would expect a decrease in the magnitudes of those quantities, also leading to an increased interdiffusion due to the decrease of diffusion-potential terms that depend on stress. However, plastic deformation will not completely compensate the effect of stress-hampered interdiffusion since an elastic stress on the level of the yield stress will remain.

### III. REAL-TIME ANALYSIS OF INTERDIFFUSION

To compare the modeled interdiffusion with experimental data, we performed in-situ EDXRD measurements during the selenization of metallic Cu-In-Ga precursors with subsequent annealing. Similar to standard angle-dispersive x-ray diffraction, EDXRD is sensitive to lattice plane distances and hence to expansions or contractions of the lattice caused by compositional changes, allowing us to make conclusions about the extent of interdiffusion and

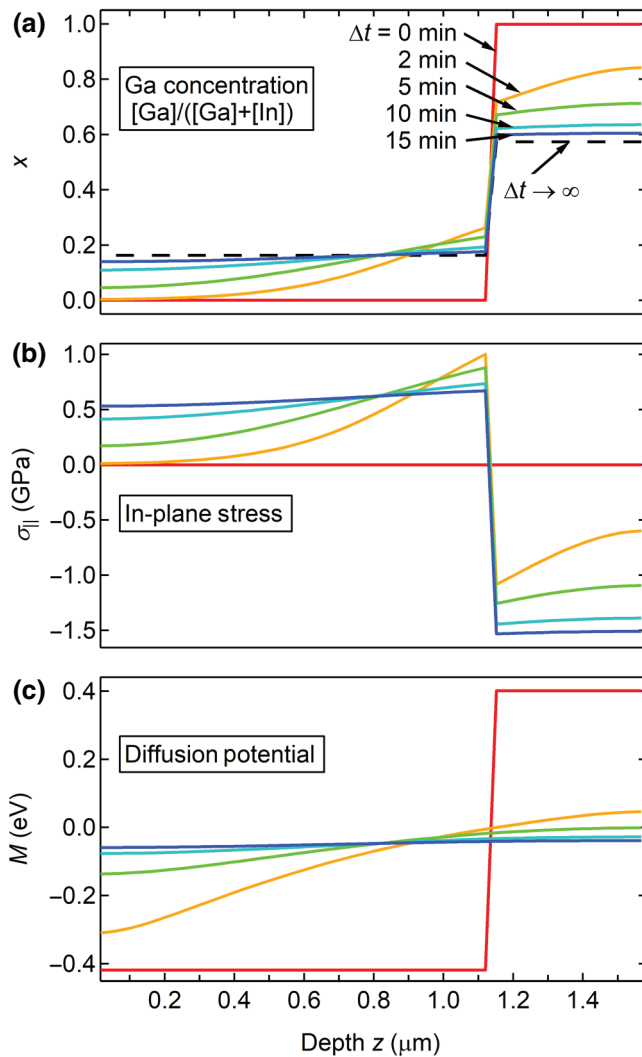


FIG. 3. Modeling of In-Ga interdiffusion under the influence of stress formation based on input parameters from the literature. (a) Ga distribution,  $x = [\text{Ga}]/([\text{Ga}]+[\text{In}])$ . (b) In-plane stress distribution,  $\sigma_{||}(z)$ . (c) Diffusion potential,  $M(z)$ . Each quantity is plotted for different simulation times. The dashed line in (a) shows the analytical steady-state solution. See Appendix E for details.

thus about the evolution of Ga and In profiles along the layer thickness over time.

### A. Experimental details

Real-time EDXRD analysis is performed at the energy dispersive diffraction (EDDI) beamline at the synchrotron facility BESSY II at the Helmholtz-Zentrum Berlin, Germany [57]. An in-situ reaction chamber is used to perform the selenization process [24] of a metallic Cu-In-Ga multilayer precursor [58] and to survey the subsequent interdiffusion inside the resulting CIGS absorber layer. The multilayer Cu-In-Ga precursor film consisting of 22 In/Cu-Ga/In triple layers with total thickness of

700 nm and a composition of  $[\text{Cu}]/([\text{In}] + [\text{Ga}]) = 0.87$  and  $[\text{Ga}]/([\text{In}] + [\text{Ga}]) = 0.27$  is deposited by dc sputtering onto a Mo-covered soda-lime substrate. The substrate has a thickness of 3.1 mm and the Mo layer a thickness of 1  $\mu\text{m}$ . The selenization of the Cu-In-Ga precursor resulted in a CIGS film with a thickness of about 2  $\mu\text{m}$ . The substrate temperature is controlled by a thermocouple above the substrate and raised to 600  $^{\circ}\text{C}$  with a heating rate of 200 K/min. The temperature is held constant for 12 min at 600  $^{\circ}\text{C}$  [see Fig. 4(a)]. EDXRD data is recorded with an energy-dispersive high-purity Ge detector with a time resolution down to 3 s per spectrum under a diffraction angle of  $2\theta = 6.08$ . For more details on the setup, see Ref. [59].

The two CIGS 112 reflections visible in the spectra are fitted to Gaussian functions using simulated annealing [60].

### B. Selenization and interdiffusion

Color-coded EDXRD intensities as a function of photon energy and process time recorded during selenization of a Cu-In-Ga precursor and subsequent annealing are plotted in Fig. 4(b). The evolution of temperature during the process is shown in Fig. 4(a). The measurement starts with the onset of the heating of the precursor together with elemental Se, followed by a transition of the initial metallic phases (not shown) to binary selenide phases and finally to the chalcopyrite CIGS phase. For a detailed description of the phase formation, see Ref. [10]. At  $t_0 \approx 11$  min [vertical dotted line in Figs. 4(a)–4(c)] the selenization process of the absorber is finished. This is indicated by observing that the simultaneously recorded Se  $K\alpha$  fluorescence signal [Fig. 4(c)]—after a steep rise—stays constant beyond that point in time. At  $t_0$ , two distinctive 112 reflections can be discerned [Figs. 4(a) and 4(d)], which coincide with the expected positions of the CIS ( $\text{CuInSe}_2$ ) 112 and CGS ( $\text{CuGaSe}_2$ ) 112 diffraction signals at 600  $^{\circ}\text{C}$  (see Appendix A for details). Since CIS has a larger unit cell than CGS [44], the diffraction signal of CIS 112 lies at lower photon energies than CGS 112.

The 112 signals in Fig. 4 can be seen to initially converge over time, which can be explained by In-Ga interdiffusion [61]. Eventually, however, the convergence slows down considerably after some minutes and the signals remain separated by a constant energy difference, which indicates stagnation of the In-Ga interdiffusion.

### C. Fitting the model to real-time data

To compare the interdiffusion model to the experimental data, we calculated the EDXRD signals for the Ga distributions predicted by the model for each time step. The resulting CIGS 112 signal is the superposition of the attenuated signals emerging from the different layer depths (see Appendix A for details). The energy of the resulting intensity maxima of the Ga- and In-rich signals is

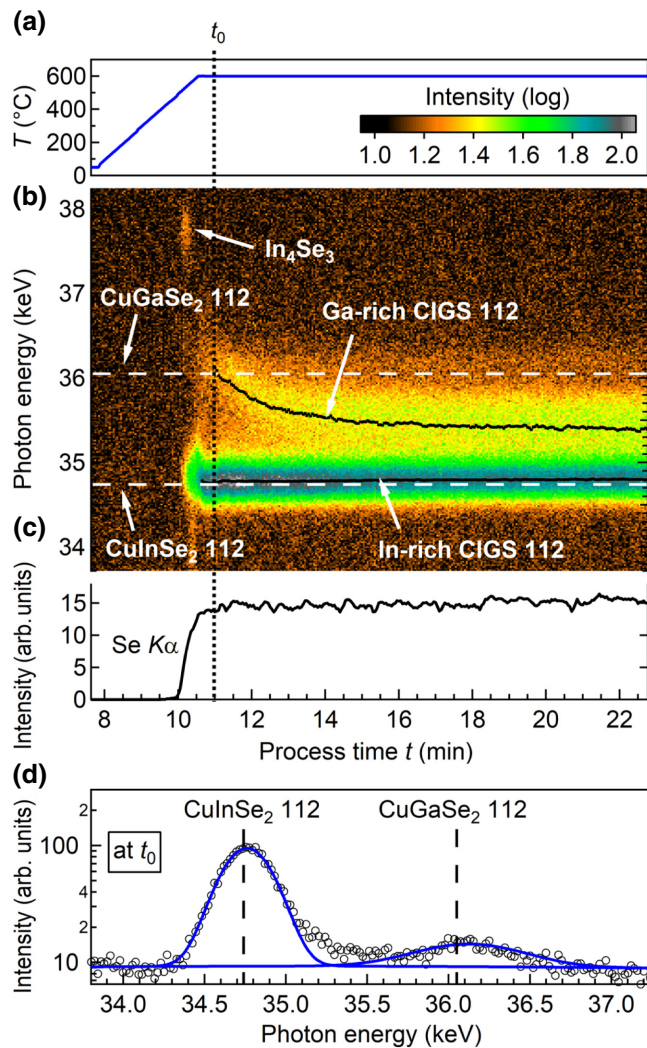


FIG. 4. (a) Process temperature over time. (b) Normalized color-coded EDXRD intensities as a function of process time and photon energy as measured during selenization of a Cu-In-Ga precursor layer with an integral GGI of 0.27. The dashed horizontal lines show the expected energies of the 112 diffraction at 600°C of pure CIS and CGS phases ( $E_{\text{CIS}} = 34.74$  keV and  $E_{\text{CGS}} = 36.06$  keV). (c) Simultaneously measured Se  $K\alpha$  fluorescence intensity. (d) EDXRD intensities as a function of photon energy at process time  $t_0$ .

then compared to the measured position of the intensity maxima of the In- and Ga-rich CIGS 112 signals, which are extracted from measured spectra using a double-peak Gauss-curve fit.

The energies of the In- and Ga-rich 112 maxima extracted from the measured real-time EDXRD data [Fig. 4(b)] are depicted in Fig. 5(a) as open circles. The red lines represent the expected evolution assuming pure Fickian diffusion, fitted to the data between the two vertical lines ( $t_0 = 11$  min and  $t_1 = 14$  min). The used parameter values can be found in Table I, with Young's modulus set to  $Y = 0$  GPa and the diffusion coefficient used as a

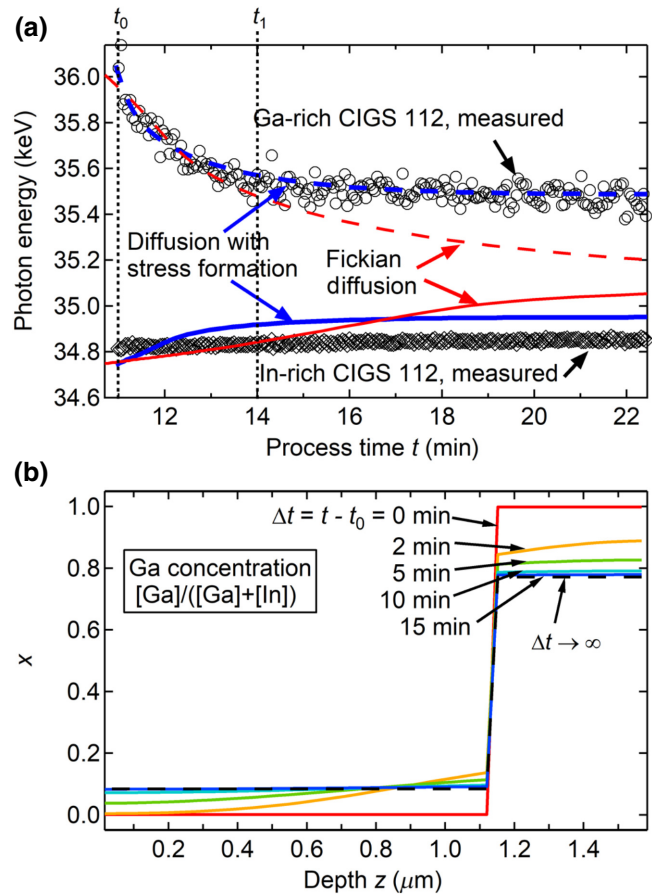


FIG. 5. (a) Comparison of measured (black) and simulated CIGS 112 peak positions using a standard Fickian-type diffusion model (red) and the stress-comprising diffusion model (blue). Vertical lines indicate the measurement interval between  $t_0 = 11$  min and  $t_1 = 14$  min used to fit the standard Fickian diffusion model to the data. (b) Ga distribution over the absorber layer thickness for different times corresponding to the simulation with the stress-comprising diffusion model. The dashed line shows the analytical steady-state solution.

fit parameter. While at the beginning of the interdiffusion a good fit between pure Fickian diffusion and the experimental data can be obtained, beyond the vertical line at  $t_1$  the model strongly deviates from the data. The diffusion coefficient resulting in the best fit is found to be  $D^F \approx 9.76 \times 10^{-12}$  cm<sup>2</sup>/s.

A Fickian diffusion process is characterized by the interdiffusion being solely driven by intrinsic concentration gradients in the thin film. This leads to the process carrying on until a complete intermixing of Ga and In is achieved. Because the unit-cell volume of CIGS is assumed to depend on the local GGI value, a uniform Ga distribution leads to a uniform unit-cell volume throughout the absorber. Consequently, the simulation will predict a single 112 signal after a sufficient annealing time. The constant separation of the measured In-rich and Ga-rich CIGS 112



signals in Fig. 5(a) can therefore not be explained by standard Fickian diffusion.

Better agreement between observation and model can be achieved using the interdiffusion model comprising build-up of in-plane stresses [Eqs. (8) with (11)]. We assume that after film growth—that is, at the onset of interdiffusion—the absorber is in a stress-free state. Subsequently developing in-plane stresses will, due to the Poisson relation, lead to out-plane strains that also have to be considered when predicting the emergent EDXRD signals (see Appendix A for details).

Fitting of the model comprising stress [blue curve in Fig. 5(a)] to the measurement [open circles in Fig. 5(a)] is done using the tracer-diffusion coefficient  $D^*$  of In and Ga and additionally Young's modulus,  $Y$ , as free parameters. All other parameters are fixed to the values given in Table I. It can be seen from Fig. 5(a) that the stagnation of the convergence of the In-rich and Ga-rich CIGS 112 signals is well reproduced by the model. The corresponding Ga gradient ultimately converges to a steady and nonflat state, as is shown in Fig. 5(b). In Fig. 5(b) we also show (dashed black line) the approximate steady-state solution to the interdiffusion problem comprising build-up of stress found in Appendix E. It can be seen that the analytical approximation very well reproduces the final Ga distribution.

The parameter optimization yields a Young modulus of  $Y_O = 231$  GPa and a tracer-diffusion coefficient of  $D_O^* = 1.9 \times 10^{-11} \text{ cm}^2 \text{ s}^{-1}$ . [The resulting relative peak differences are shown in Fig. 6(a).] We recall that the literature values for the tracer-diffusion coefficients of In and Ga vary greatly over different orders of magnitude, from  $10^{-11}$  to  $10^{-14} \text{ cm}^2 \text{ s}^{-1}$  [13,16,17,49,50]. The diffusion coefficient  $D_O^*$  lies within this expectable range. The predicted Young modulus, however, is significantly higher than previously reported values,  $Y = 68.9$  GPa [51].

The deviation of the determined Young modulus from reported values is influenced by the assumed enthalpy of mixing. With a higher enthalpy of mixing leading to smaller predicted Young's moduli. Moreover, further simplifications that are employed when developing the interdiffusion model can affect its predictions. For example, we neglect influences by the microstructure—such as grain boundaries, lattice misfits, or lateral inhomogeneities—as well as the influence of vacancies on the diffusion process. Vacancies will enter the picture because of differing activation energies for the migration of Ga and In in CIGS. The migration barrier for In in CGS is predicted to be lower than the migration barrier for Ga in CIS [8]. This results in larger diffusion coefficients for In than for Ga. These deviating diffusion coefficients will, in effect, lead to a net flux of vacancies. A smaller diffusion coefficient for Ga in CIS can also be expected to lead to a slower increase of the In-rich 112 signal and hence to an improved fit between the simulated and measured In-rich 112 peak

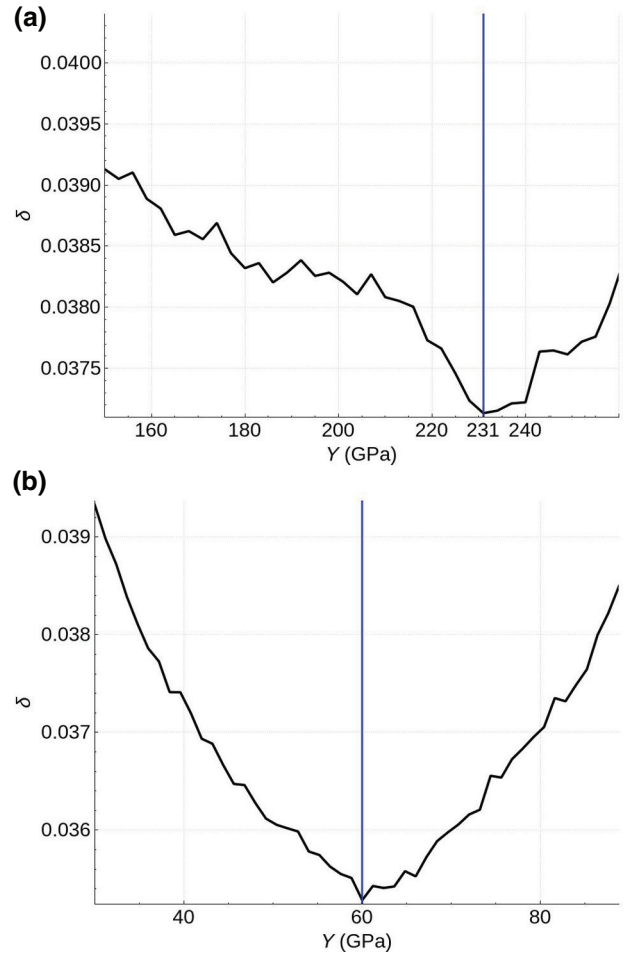


FIG. 6. (a) Relative differences,  $\delta(D_O^*, Y)$ , for the full model comprising out-plane strain according to Eq. (3) as a function of Young's modulus. A minimum occurs at  $Y_O = 231$  GPa and  $D_O^* = 1.9 \times 10^{-11} \text{ cm}^2/\text{s}$ . (b) Relative differences for the simulation using the averaged in-plane stress,  $\langle \sigma_{\parallel} \rangle$ , in Eq. (3) instead of  $\sigma_{\parallel}$ . A minimum is reached at  $Y_O^{(\sigma_{\parallel})} = 60$  GPa and  $D_O^{*(\sigma_{\parallel})} = 9.32 \times 10^{-12} \text{ cm}^2/\text{s}$ .

positions in Fig. 5(a). However, the vacancies are not expected to have a large effect on the predicted Young modulus due to vacancies only being present in relatively low numbers (see Sec. IID), and because the vacancies themselves are expected to be close to chemical equilibrium due to the presence of grain boundaries, surfaces, and interfaces [41].

Furthermore, we neglect the anisotropy of the material, although CIGS crystallizes in the tetragonal crystal structure and is thus anisotropic [55,62]. This anisotropy will lead to nontrivial average values for the material parameters, dependent on the texture of a specific sample [63]. The EDXRD measurement only probes crystallites with the 112 plane oriented parallel to the sample surface. The Young modulus in 112 direction—95 GPa for CGS and 77 GPa for CIS, as calculated by Voigt and Reuss methods

[63] from the elastic coefficient tensor [55,62]—is larger than the mean Young modulus (approximately 70 GPa) used for the modeling.

The surface of the thin film as well as the interface between the In-rich and Ga-rich regions are expected to exhibit roughness [10]. This means that the Ga gradient and hence the direction of the diffusion-induced stress is not everywhere parallel to the normal of the 112 plane probed by the EDXRD measurement. Hence, the effect of the calculated out-plane strain on the 112 peak positions could be overestimated. Furthermore, the interface between CIGS and Mo thin films may not be perfectly coherent and exhibit gaps that might lead to further stress reduction and, in an extreme case, to delamination, which, however, is not observed here.

Also, the elastic material parameters may be different at grain boundaries in comparison to their bulk values. However, because the volume of grain boundaries is much smaller than the bulk volume, this influence may be neglected in a first approximation.

If the stress becomes so large that it induces microstructural changes, such as grain boundary migration or formation of dislocations, i.e., plastic deformation takes place, the assumptions of linear elasticity are no longer valid, which will influence numerical predictions, as discussed in Sec. II E.

Additionally, we would like to mention that if the out-plane strain is calculated in dependence of the averaged in-plane stress over the thin film,  $\langle\sigma_{\parallel}\rangle$ , in Eq. (3) in place of  $\sigma_{\parallel}$ , the fit of the model to the experimental data results in  $Y_O^{(\sigma_{\parallel})} = 60$  GPa, lying slightly below the reported value of approximately 70 GPa.

#### IV. DISCUSSION

Our model enables us to calculate the stress formed by the interdiffusion of differently sized atomic species in thin films constrained by a rigid substrate. By considering the elastic work that needs to be performed in this process on the crystal lattice we show how this build-up of stress hampers interdiffusion. For the In-Ga interdiffusion in CIGS, our results show that the interplay of stress formation and interdiffusion results in a stable composition gradient. This gradient cannot be further reduced by a prolonged annealing time, but only by intentionally designing the conditions for chemical equilibrium that establish inside the thin film. One way to achieve this is by altering the state of stress of the sample. While in the case of sequential processing of  $\text{Cu}(\text{In,Ga})\text{Se}_2$ , the stagnation of the In-Ga interdiffusion at very steep GGI gradients is undesirable, establishing and maintaining compositional gradients for an optimal bandgap profile is a general problem occurring with a whole range of thin-film light-absorbing structures. The values employed for the calculations in this work are specific for CIGS. However, the equations of

the presented model are general for all thin-film compounds containing differently sized isovalent atomic pairs deposited on rigid substrates. Therefore, our model has the potential to provide a better understanding of the interconnection between interdiffusion of differently sized atoms and the formation of stresses for various materials. For perovskites, it is known that material gradients and strains are interconnected [64] and influence the charge carrier dynamics and energy band bending [26,27], as well as charge collection and recombination [65]. Also, the Se-to-S ratio in  $\text{Cu}(\text{In,Ga})(\text{S,Se})_2$  (CIGSSe) solar cell absorbers is known to influence the device parameters and is regularly designed by interdiffusion processes of Se and S [21,22]. Furthermore, the structural and electronic properties of  $\text{Cu}_2\text{ZnSn}(\text{S,Se})_4$  kesterites are also well known to be composition dependent [23,66] and compositional gradients are often obtained by exploiting interdiffusion processes of Se and S [24,67,68] and Ge and Sn [25]. Through changing fabrication techniques and substrates, stress-hampered interdiffusion may be exploited to intentionally design stress fields that lead to stable and optimal composition gradients.

#### V. CONCLUSIONS

We show that the persistent character of nonoptimal Ga and In gradients inside CIGS absorber layers produced in the sequential fabrication process can be explained by the formation of stress induced by the thin film's rigid substrate during the interdiffusion of differently sized Ga and In atoms. This build-up of stress hampers interdiffusion since elastic work needs to be performed on the crystal lattice. The resulting stable composition gradient cannot be further reduced by extended annealing time, but, e.g., by influencing the yield stress via a change in temperature, affecting the stress state of the material. In the case of  $\text{Cu}(\text{In,Ga})\text{Se}_2$ , but also for other materials, a stagnation of interdiffusion at nonoptimal gradients is undesirable, and understanding the interplay between stress and interdiffusion may be exploited to intentionally design stress fields that lead to optimized and stable compositional gradients.

#### ACKNOWLEDGMENTS

Financial support by the Helmholtz Virtual Institute Microstructure Control in Thin-Film Solar Cells, VI-520, by the EMPIR programme co-financed by the Participating States and by the European Union's Horizon 2020 research and innovation programme via the project HyMET (16ENG03), and by the German Federal Ministry for Economic Affairs and Energy (BMWi) via the project EFFCIS (0324076B) is gratefully acknowledged. Special thanks go to Guido Wagener, Manuela Klaus, Jan-Peter Bäcker, Sergej Levcenco, and Tim Kodalle for their support before and during the beamtime, and to Karsten Albe for discussion and helpful comments.

## APPENDIX A: SIMULATION OF IN-SITU EDXRD DATA

Because we measure the 112 diffraction peaks in an energy-dispersive setting, the unit cells producing these signals are oriented with their 112 planes perpendicular to the out-plane direction of the sample. As such, any effective out-plane strain has to be applied to the 112 plane distances. That is, if we denote the distance of the 112 planes in the stress-free state by  $d'_{112}(x)$  then the 112 plane distance in the actual state,  $d_{112}$ , after application of the effective out-plane strain, can be calculated by

$$d_{112} = d'_{112}(1 + \epsilon_{\perp}), \quad (\text{A1})$$

$$d'_{hkl} = \frac{V_{\text{UC}}}{\sqrt{(hac)^2 + (kac)^2 + (la^2)^2}}, \quad (\text{A2})$$

where  $a(x)$  and  $c(x)$  are given by Eqs. (18) and (19).

The diffraction energy  $E(x)$  for a layer with GGI  $x$  then follows using the energy dispersive Bragg formula with the lattice spacing given by Eq. (A1) and the  $2\Theta$  angle as in Table I:

$$E(x) = \frac{hc}{2d(x) \sin(\Theta)}. \quad (\text{A3})$$

Here  $E(x)$  is the energy at which the diffracted signal is maximal and  $c$  and  $h$  are the velocity of light and Planck's constant, respectively.

The resulting signal intensity distribution is modeled as a Gauss curve centered around  $E(x)$ . Such determined signals emerging from the different sublayers are then attenuated according to their depth in the thin film, since the layers on top will absorb part of the diffracted signal, depending on the atomic cross sections of the material. The resulting signals are superimposed and the detector broadening is taken into account, producing the simulated EDXRD signal [69].

This method produces two distinct 112 diffraction signals, one belonging to the signal emergent from layers with a high GGI and one to layers with low GGI. The energies at which the maximal diffraction intensities occur for those two signals are then extracted, resulting in the simulated 112 signal peak positions for the Ga- and In-rich parts of the layer,  $E_S^k$  with  $k \in [\text{Ga}, \text{In}]$ .

## APPENDIX B: PARAMETER OPTIMIZATION

Obtaining the peak positions  $E_S^k$  of both simulated reflections and the measured peak positions  $E_M^k$  allows for comparison of simulation and measurement by introduction of the relative peak position difference,  $\delta(D^*, Y)$ , as a

cost function:

$$\delta^2(D^*, Y) = \frac{1}{2N_S} \sum_{(t,k)} \left( \frac{E_M^k - E_S^k}{E_M^k} \right)^2. \quad (\text{B1})$$

The sum in Eq. (B1) runs over both 112 reflections, counted by  $k \in [\text{Ga}, \text{In}]$ , and over all recorded spectra,  $t \in [1, N_S]$ .

The cost function will depend on both  $Y$  and  $D^*$  since they are the only free parameters. By minimizing  $\delta$ , we can then find optimal parameter values. The diffusion equation is numerically solved for a Young modulus and then a best-fitting diffusion coefficient is searched for by minimizing  $\delta$ . Because of the linearity of the underlying diffusion equation, (8) only needs to be solved for one pair  $(Y, D^*)$  to produce all solutions for  $(Y, \lambda D^*)$ ,  $\lambda \in \mathbb{R}^+$ .

We implemented a simulated annealing scheme [60] comprising an exponential cooling to effectively search the available parameter space for optimal values for a given measurement.

## APPENDIX C: DIFFUSION POTENTIAL

We follow the derivation of Voorhees *et al.* [39] and show Eq. (11) in detail from the differential of the Gibbs potential, Eq. (9). First, we set  $dT = 0$  in Eq. (9), giving

$$dg = -\epsilon_{ij} d\sigma_{ij} + M \rho dx. \quad (\text{C1})$$

The Maxwell relation for (C1) reads

$$\frac{\partial \epsilon_{ij}}{\partial x} \Big|_{\sigma} = - \frac{\partial M \rho}{\partial \sigma} \Big|_x. \quad (\text{C2})$$

The subscript next to the partial derivatives indicates which variable is to be held constant. We now have to find a relation connecting the strain to the stress. For that purpose, we write down Hook's law in general form,

$$\sigma_{ij} = C_{ijkl}(\epsilon_{ij} - \epsilon_{ij}^E). \quad (\text{C3})$$

We employ the Einstein notation, summing over any index appearing twice in a term. Here  $\epsilon_{ij}^E$  denotes the eigenstrain, that is, the strain that has to be applied to the system to transform it into a stress-free state, and  $C_{ijkl}$  is the stiffness tensor, whose inverse,  $S_{ijkl}$ , is called the compliance tensor. Inverting Eq. (C3) gives

$$\epsilon_{ij} = S_{ijkl} \sigma_{kl} + \epsilon_{ij}^E. \quad (\text{C4})$$

Inserting Eq. (C4) into Eq. (C2) and remembering that the stress is to be held constant during the derivative gives

$$\frac{\partial S_{ijkl}}{\partial x} \sigma_{kl} + \frac{\partial \epsilon_{ij}^E}{\partial x} = - \frac{\partial (M \rho)}{\partial \sigma} \Big|_x. \quad (\text{C5})$$

Next, we integrate Eq. (C5) from the stress-free state to the stress state  $\sigma_{ij}$ , giving

$$M(\sigma_{ij}) = M^0 - \frac{1}{\rho} \left\{ \overbrace{\frac{\partial S_{ijkl}}{\partial x} \sigma_{ij} \sigma_{kl}}{=:M^S} + \overbrace{\frac{\partial \epsilon_{ij}^E}{\partial x} \sigma_{ij}}{=:M^\epsilon} \right\}. \quad (\text{C6})$$

Here,  $M^0$  is the diffusion potential for vanishing stress, given by Eq. (12), and  $M^S$  and  $M^\epsilon$  are the diffusion potential contributions from variable elastic parameters and variable strain, respectively.

If we assume that the elastic coefficients do not depend on composition then  $M^S$  vanishes. Furthermore, the only nonvanishing stress components are in the in-plane direction,  $\sigma_{\parallel}$ . In this direction the eigenstrain is connected to the in-plane strain  $\epsilon_{\parallel}$  by

$$\epsilon_{\parallel}^E = -\epsilon_{\parallel}. \quad (\text{C7})$$

Because there are two independent in-plane directions, we can finally transform Eq. (C6) to

$$M(\sigma) = M^0 + \frac{2}{\rho} \frac{\partial \epsilon_{\parallel}}{\partial x} \sigma_{\parallel}. \quad (\text{C8})$$

This is equivalent to Eq. (11). To determine  $M^0$ , the diffusion potential in the stress-free state, we use  $d\sigma_{ij} = 0$  in Eq. (9) and calculate

$$M^0(x) = \frac{1}{\rho} \frac{\partial g(x, \sigma_{ij} = 0)}{\partial x} = \frac{1}{\rho} \frac{\partial g^0(x)}{\partial x}. \quad (\text{C9})$$

Here  $g^0$  is the Gibbs free energy density for a CIGS system not subject to any stresses and strains.

We conclude this section by estimating the magnitude of the additional diffusion potential term that results if the elastic coefficients depend on composition. The material is assumed to be isotropic and the elastic compliance tensor can be written as  $S = (1 - \nu)/Y$ . Furthermore, we assume that the elastic parameters  $Y$  and  $\nu$  depend linearly on composition  $x$ :

$$Y(x) = Y_1 x + (1 - x) Y_2 = Y_2 + \overbrace{\Delta Y}^{=:Y_1 - Y_2} x, \quad (\text{C10})$$

$$\nu(x) = \nu_1 x + (1 - x) \nu_2 = \nu_2 + \underbrace{\Delta \nu}_{=: \nu_1 - \nu_2} x. \quad (\text{C11})$$

We can then estimate the relative magnitude of  $M^S$  to be

$$\begin{aligned} \frac{M^\epsilon}{M^S} &= 2 \frac{\epsilon_x}{S_x} \frac{1}{\sigma} \\ &= 2 \frac{1 - \nu}{Y} \frac{Y^2}{\Delta \nu Y + (1 - \nu) \Delta Y} \\ &= - \frac{2}{\underbrace{\Delta \nu / (1 - \nu)}_{=:x_\nu} + \underbrace{\Delta Y / Y}_{=:x_Y}} \\ &= - \frac{2}{x_\nu + x_Y}. \end{aligned} \quad (\text{C12})$$

Measurements of the elastic material parameters for CIS and CGS usually give a range of Young's moduli of between 2 and 20 GPa and a relative change of Poisson's ratios of around 0.01 [54–56]. This results in relative differences  $M^\epsilon/M^S$  of the diffusion potential contributions of approximately 70 to 10, respectively. This further confirms that to a good approximation the influence of compositional-dependent elastic parameters can be neglected in this study.

#### APPENDIX D: PHENOMENOLOGICAL COEFFICIENT

We will derive Eq. (7) for the phenomenological coefficient of diffusion in a binary system comprising the effects of stress formation.

Manning [36] showed that the equation for the flux of a species  $i$ ,  $J_i$ , in a diffusing system composed of two components that are under the influence of driving forces other than the concentration gradient and that have the same tracer-diffusion coefficient,  $D^*$ , is given by

$$J_i = -D^* \left( 1 + \underbrace{\frac{x_i}{x_{i,z}} \frac{\partial \ln \gamma_i}{\partial z}}_{=: \alpha} \right) \rho x_{i,z}. \quad (\text{D1})$$

The symbol  $x_{i,z}$  indicates the partial derivative of  $x_i$  with respect to  $z$ ,  $\alpha$  is the thermodynamic factor, and  $\gamma_i$  is the activity coefficient of species  $i$ . The activity coefficient is defined as the part of the chemical potential not arising from the entropy of mixing. For example, the chemical potential of species  $i$ ,  $\mu_i$ , is given by

$$\mu_i = \mu_i^0 + kT \ln(\gamma_i x_i), \quad (\text{D2})$$

where  $\mu_i^0$  is the constant chemical potential for pure species  $i$ , which can be omitted in the following since we deal with derivatives of chemical potentials.

We first calculate a relation between the spatial gradients of the activity coefficients for different species. This relation will then help us to bring Eq. (5) into the form (D2), resulting in an equation for  $L$ .



With the help of the Gibbs-Duhem equation for a two-component system, we calculate

$$\begin{aligned} x_1 d\mu_1 + x_2 d\mu_2 &= 0, \\ \Rightarrow x_1 \frac{\partial \mu_1}{\partial z} + x_2 \frac{\partial \mu_2}{\partial z} &= 0. \end{aligned} \quad (\text{D3})$$

With Eq. (D2) we derive a relation for the spatial gradient of  $\mu_i$ ,

$$\frac{\partial \mu_i}{\partial z} = kT \left( \frac{\partial \ln \gamma_i}{\partial z} + \frac{1}{x_i} x_{i,z} \right). \quad (\text{D4})$$

Using Eq. (D4) together with Eq. (15) in Eq. (D3) finally gives

$$x_1 \frac{\partial \ln \gamma_1}{\partial x_1} = -x_2 \frac{\partial \ln \gamma_2}{\partial x_2}. \quad (\text{D5})$$

We now evaluate Eq. (5) using the definition of  $M$  given by Eq. (10) and the spatial gradients of the chemical potential  $\mu_i$  given by Eq. (D4). This results in

$$\begin{aligned} J_i &= -L \nabla_z M \\ &= -LkT \left\{ \frac{1}{x_1} x_{1,z} - \frac{1}{x_2} x_{2,z} + \frac{\partial \ln \gamma_1}{\partial z} - \frac{\partial \ln \gamma_2}{\partial z} \right\}. \end{aligned} \quad (\text{D6})$$

In the next step we make use of the relations  $x_1 + x_2 = 1$ , Eq. (D5), and  $x_{1,z} = -x_{2,z}$ . The result reads

$$J_i = -LkT \left( 1 + \frac{x_i}{x_{i,z}} \frac{\partial \ln \gamma_i}{\partial z} \right) \frac{1}{x_1 x_2} x_{i,z}. \quad (\text{D7})$$

From Eq. (D5) and  $x_{1,z} = -x_{2,z}$  it is easily seen that

$$\frac{x_i}{x_{i,z}} \frac{\partial \ln \gamma_i}{\partial z} := \frac{x_1}{x_{1,z}} \frac{\partial \ln \gamma_1}{\partial z} = \frac{x_2}{x_{2,z}} \frac{\partial \ln \gamma_2}{\partial z}. \quad (\text{D8})$$

Using this result in Eq. (D7), we arrive at

$$J_i = -LkT \left( 1 + \frac{x_i}{x_{i,z}} \frac{\partial \ln \gamma_i}{\partial z} \right) \frac{1}{x_1 x_2} x_{i,z}. \quad (\text{D9})$$

Comparison of Eq. (D9) with Eq. (D1) results in the phenomenological coefficient

$$L = \frac{D^* \rho}{kT} x_1 x_2 = \frac{D^* \rho}{kT} x_1 (1 - x_1). \quad (\text{D10})$$

## APPENDIX E: APPROXIMATE STEADY-STATE SOLUTION

We show how to find the approximate steady-state solution to the diffusion equation (8) and start by noting that a steady state is characterized by a vanishing flux. The flux is

given by Eq. (5), the vanishing of which is equivalent to the vanishing of the spatial gradient of the diffusion potential  $M(x, x_0)$  [Eq. (11)]:

$$M_z = M_x(x^\infty, x_0) x_z^\infty + M_{x_0}(x^\infty, x_0) x_{0,z} = 0. \quad (\text{E1})$$

Here,  $x^\infty(z)$  denotes the steady-state solution after an infinite amount of time. This equation has to hold for all layer depths  $z$ . As in the previous section, a subscript indicates a partial derivative with respect to the corresponding variable, e.g.,  $M_z \equiv \partial M / \partial z$ .

Using the decomposition of  $M$  into stress-independent and stress-dependent parts,  $M^0(x)$  and  $M^\sigma(x, x_0)$ , according to Eq. (11) gives

$$0 = (M_x^0 + M_x^\sigma) x_z^\infty + M_{x_0}^\sigma x_{0,z}. \quad (\text{E2})$$

We assume that the initial Ga distribution is a step function, so that the derivative  $x_{0,z}$  takes a delta-function form:

$$x_{0,z} \equiv \frac{dx_0}{dz} = \Delta x_0 \delta(\lambda d - z). \quad (\text{E3})$$

Here  $d$  is the thickness of the system,  $\lambda$  is the total GGI of the sample, and  $\Delta x_0$  is the initial GGI difference between the Ga- and In-rich parts of the absorber, that is, the step size of the initial GGI distribution.

Now, if the initial Ga distribution is of step function type then so is the steady-state solution  $x^\infty(z)$ . To see this, evaluate Eq. (E2) at some  $\bar{z} \neq \lambda d$  such that  $x_{0,z}(\bar{z}) = 0$ . If we suppose that  $x_z^\infty \neq 0$  then, in order for Eq. (E2) to vanish, we must have

$$M_x^0[x^\infty(\bar{z})] = -M_x^\sigma[x^\infty(\bar{z}), x_0(\bar{z})]. \quad (\text{E4})$$

In the small strain approximation the strain, Eq. (1), can, to a good approximation, be written as a linear function of  $(x - x_0)$ , that is,

$$\epsilon = \epsilon^1 + \epsilon^2(x - x_0), \quad (\text{E5})$$

where  $\epsilon^1$  and  $\epsilon^2$  are some constants determined by the used stress model. The function  $M^\sigma$  therefore also depends linearly on  $x$  and the derivative  $M_x^\sigma$  is a constant. Consequently, solving Eq. (E4) will lead to a solution of the form  $x^\infty(\bar{z}) = \text{const}$  for all layer depths. However, such a solution is in disagreement with the stress leading to a nonuniform final Ga distribution. As such, in order for Eq. (E2) to vanish at a point  $\bar{z}$  with  $x_{0,z}(\bar{z}) = 0$ , we must have  $x_z^\infty(\bar{z}) = 0$  and, for  $\bar{z} = \lambda d$ , we have  $x_{0,z}(\bar{z}) \neq 0$  and  $x_z^\infty(\bar{z}) \neq 0$ . This is equivalent to  $x^\infty(z)$  having step function form. Denoting the final GGI step size of the sample

as  $\Delta x^\infty$ , we can write

$$\frac{dx^\infty}{dz} = \Delta x^\infty \delta(\lambda d - z). \quad (\text{E6})$$

Substituting Eqs. (E6) and (E3) into Eq. (E2) and integrating over the layer thickness gives

$$\begin{aligned} \Delta x^\infty &= -\frac{M_{x_0}^\sigma(\bar{x}^\infty, \bar{x}_0)}{M_x^0(\bar{x}^\infty) + M_x^\sigma(\bar{x}^\infty, \bar{x}_0)} \Delta x_0 \\ &\equiv -\Theta(\bar{x}^\infty) \Delta x_0. \end{aligned} \quad (\text{E7})$$

Here  $\bar{x}^\infty$  and  $\bar{x}_0$  denote the GGI at the point  $\bar{z} = \lambda d$  for the steady state and the initial solution, respectively. We now denote the GGI values in the Ga- and In-rich parts of the layer in the initial state by  $x_G^0$  and  $x_I^0$  and in the steady state by  $x_G^\infty$  and  $x_I^\infty$ . Because  $\bar{x}^\infty$  and  $\bar{x}_0$  are evaluated at the jump point of the step functions, they can be chosen as the average GGI values between the In- and Ga-rich layers, that is,

$$\bar{x}_0 = \frac{1}{2}(x_G^0 + x_I^0), \quad (\text{E8})$$

$$\bar{x}^\infty = \frac{1}{2}(x_G^\infty + x_I^\infty), \quad (\text{E9})$$

where  $\bar{x}_0$  is given by the initial GGI distribution, but  $\bar{x}^\infty$ , on the other hand, is not known *a priori*.

To proceed, we can express the mass conservation with the help of the so far introduced quantities. The total GGI  $\lambda$  is given as the weighted sum of the GGI values in the In- and Ga-rich layers, which are  $(1 - \lambda)d$  and  $\lambda d$  thick, respectively. So we have

$$\lambda = \lambda x_G^\infty + (1 - \lambda)x_I^\infty. \quad (\text{E10})$$

After some algebra, Eq. (E10) together with  $\Delta x^\infty = x_G^\infty - x_I^\infty$  leads to

$$\bar{x}^\infty = \lambda + \frac{1}{2}(1 - 2\lambda)\Delta x^\infty. \quad (\text{E11})$$

We can now substitute Eq. (E7) into Eq. (E11) to obtain

$$\bar{x}^\infty = \lambda - \frac{1}{2}(1 - 2\lambda)\Theta(\bar{x}^\infty)\Delta x_0. \quad (\text{E12})$$

In Eq. (E12)  $\bar{x}^\infty$  appears on the left- and right-hand sides and closed-form solutions are only possible for certain functional dependencies of  $\Theta(\bar{x}^\infty)$ . In general, numerical root-finding algorithms have to be used to solve for  $\bar{x}^\infty$ . On the other hand, inspection of the equation suggests that the right-hand side of Eq. (E12) is, in the parameter space of interest, a contracting mapping, thus making it possible to apply the Banach fixed-point theorem and use the relation to obtain an iterative solution.

A good first guess for the average GGI value at the jump point is the total GGI value of the sample,  $\bar{x}_0^\infty = \lambda$ , since this is the value approached for vanishing Young's moduli. The iterative procedure can be explicitly stated as

$$\bar{x}_{i+1}^\infty = \lambda - \frac{1}{2}(1 - 2\lambda)\Theta(\bar{x}_i^\infty)\Delta x_0. \quad (\text{E13})$$

Eq. (E13) leads already after the first iteration to very good agreement with the solutions obtained from numerically solving the differential diffusion equation.

The full solution,  $x^\infty(z)$ , in dependence of  $\bar{x}^\infty$  is then found by solving Eqs. (E9) and (E11) for  $x_G^\infty$  and  $x_I^\infty$ :

$$x^\infty(z) = \begin{cases} \frac{2(1 - \lambda)\bar{x}^\infty - \lambda}{1 - 2\lambda} & \text{if } z \leq \lambda d, \\ \lambda \frac{1 - 2\bar{x}^\infty}{1 - 2\lambda} & \text{if } z > \lambda d. \end{cases} \quad (\text{E14})$$

- [1] M. Nakamura, K. Yamaguchi, Y. Kimoto, Y. Yasaki, T. Kato, and H. Sugimoto, Cd-free Cu(In, Ga)(Se, S)<sub>2</sub> thin-film solar cell with record efficiency of 23.35%, *IEEE J. Photovolt.* **9**, 1863 (2019).
- [2] Chang Yan, Jialiang Huang, Kaiwen Sun, Steve Johnston, Yuanfang Zhang, Heng Sun, Aobo Pu, Mingrui He, Fangyang Liu, Katja Eder, Limei Yang, Julie M. Cairney, N. J. Ekins-Daukes, Ziv Hameiri, John A. Stride, Shiyu Chen, Martin A. Green, and Xiaojing Hao, Cu<sub>2</sub>ZnSnS<sub>4</sub> solar cells with over 10% power conversion efficiency enabled by heterojunction heat treatment, *Nat. Energy* **3**, 764 (2018).
- [3] Eui Hyuk Jung, Nam Joong Jeon, Eun Young Park, Chan Su Moon, Tae Joo Shin, Tae Youl Yang, Jun Hong Noh, and Jangwon Seo, Efficient, stable and scalable perovskite solar cells using poly(3-hexylthiophene), *Nature* **567**, 511 (2019).
- [4] Bo Yang, Ding Jiang Xue, Meiyong Leng, Jie Zhong, Liang Wang, Huaibing Song, Ying Zhou, and Jiang Tang, Hydrazine solution processed Sb<sub>2</sub>S<sub>3</sub>, Sb<sub>2</sub>Se<sub>3</sub> and Sb<sub>2</sub>(S<sub>1-x</sub>Se<sub>x</sub>)<sub>3</sub> film: Molecular precursor identification, film fabrication and band gap tuning, *Sci. Rep.* **5**, 1 (2015).
- [5] Sebastian Schleussner, Uwe Zimmermann, Timo Wätjen, Klaus Leifer, and Marika Edoff, Effect of gallium grading in Cu(In, Ga)Se<sub>2</sub> solar-cell absorbers produced by multi-stage coevaporation, *Adv. Solid State Phys.* **95**, 721 (2011).
- [6] T. Dullweber, G. Hanna, A. Shams-Kolahia, W. Schwartzlander, M. A. Contreras, R. Noufi, and H. W. Schock, Study of the effect of gallium grading in Cu(In, Ga)Se<sub>2</sub>, *Thin Solid Films* **361**, 478 (2000).
- [7] Chien Yao Huang, Wen Chin Lee, and Albert Lin, A flatter gallium profile for high-efficiency Cu(In, Ga)(Se, S)<sub>2</sub> solar cell and improved robustness against sulfur-gradient variation, *J. Appl. Phys.* **120**, 094502 (2016).
- [8] Wolfram Witte *et al.*, Gallium gradients in Cu(In, Ga)Se<sub>2</sub> thin-film solar cells, *Prog. Photovolt.: Res. Appl.* **23**, 717 (2015).
- [9] Haifan Liang, Upendra Avachat, Wei Liu, Jeroen Van Duren, and Minh Le, CIGS formation by high temperature

- selenization of metal precursors in H<sub>2</sub> Se atmosphere, *Solid State Electron.* **76**, 95 (2012).
- [10] Roland Mainz, Alfons Weber, H. Alvarez, S. Levenco, Manuela Klaus, Paul Pistor, Reiner Klenk, and Hans-Werner Schock, Time-resolved investigation of Cu(In,Ga)Se<sub>2</sub> growth and Ga gradient formation during fast selenisation of metallic precursors, *Prog. Photovolt.: Res. Appl.* **23**, 1131 (2015).
- [11] Sebastian Simon Schmidt, Christian Wolf, Humberto Rodriguez-Alvarez, and Jan-Peter Baecker, Adjusting the Ga grading during fast atmospheric processing of Cu(In,Ga)Se<sub>2</sub> solar cell absorber layers using elemental selenium vapor, *Prog. Photovolt.: Res. Appl.* **25**, 341 (2017).
- [12] Hung Ru Hsu, Shu Chun Hsu, and Yung Sheng Liu, Improvement of Voc and Jsc in CuInGaSe<sub>2</sub> solar cells using a novel sandwiched CuGa/CuInGa/In precursor structure, *Appl. Phys. Lett.* **100**, 2 (2012).
- [13] M. Marudachalam, R. W. Birkmire, H. Hichri, J. M. Schultz, A. Swartzlander, and M. M. Al-Jassim, Phases, morphology, and diffusion in CuIn<sub>x</sub>Ga<sub>1-x</sub>Se<sub>2</sub> thin films, *J. Appl. Phys.* **82**, 2896 (1997).
- [14] M. Marudachalam, H. Hichri, R. Klenk, R. W. Birkmire, W. N. Shafarman, and J. M. Schultz, Preparation of homogeneous Cu(InGa)Se<sub>2</sub> films by selenization of metal precursors in H<sub>2</sub>Se atmosphere, *Appl. Phys. Lett.* **67**, 3978 (1995).
- [15] Christian D. R. Ludwig, Thomas Gruhn, Claudia Felser, Tanja Schilling, Johannes Windeln, and Peter Kratzer, Indium-Gallium Segregation in CuIn<sub>x</sub>Ga<sub>1-x</sub>Se<sub>2</sub>: An Ab Initio-Based Monte Carlo Study, *Phys. Rev. Lett.* **105**, 025702 (2010).
- [16] Ingrid L. Repins, Steve Harvey, Karen Bowers, Stephen Glynn, and Lorelle M. Mansfield, Predicting Ga and Cu profiles in co-evaporated Cu(In,Ga)Se<sub>2</sub> using modified diffusion equations and a spreadsheet, *MRS Adv.* **2**, 3169 (2017).
- [17] Jian Wang, Ya Fei Zhang, and Jie Zhu, Diffusion coefficients of selenium and gallium during the Cu(In<sub>1-x</sub>Ga<sub>x</sub>)Se<sub>2</sub> thin films preparation process, *Adv. Mat. Res.* **815**, 448 (2013).
- [18] Fuqian Yang, Interaction between diffusion and chemical stresses, *Mater. Sci. Eng. A* **409**, 153 (2005).
- [19] S. Prussin, Generation and distribution of dislocations by solute diffusion, *J. Appl. Phys.* **32**, 1876 (1961).
- [20] James Chen-Min Li, Physical chemistry of some microstructural phenomena, *Metall. Trans. A* **9**, 1353 (1978).
- [21] B. J. Mueller, C. Zimmermann, V. Haug, F. Hergert, T. Koehler, S. Zweigart, and U. Herr, Influence of different sulfur to selenium ratios on the structural and electronic properties of Cu(In,Ga)(S,Se)<sub>2</sub> thin films and solar cells formed by the stacked elemental layer process, *J. Appl. Phys.* **116**, 174503 (2014).
- [22] Hisham Aboulfadl, Jan Keller, Jes Larsen, Lars Riekehr, Marika Edoff, and Charlotte Platzer-Björkman, Microstructural characterization of sulfurization effects in Cu(In,Ga)Se<sub>2</sub> thin film solar cells, *Microsc. Microanal.* **25**, 532 (2019).
- [23] Shiyong Chen, Aron Walsh, Ji Hui Yang, X. G. Gong, Lin Sun, Ping-Xiong Yang, Jun-Hao Chu, and Su-Huai Wei, Compositional dependence of structural and electronic properties of Cu<sub>2</sub>ZnSn(S,Se)<sub>4</sub> alloys for thin film solar cells, *Phys. Rev. B – Condens. Matter Mater. Phys.* **83**, 125201 (2011).
- [24] Roland Mainz, Bryce C. Walker, Sebastian S. Schmidt, Ole Zander, Alfons Weber, Humberto Rodriguez-Alvarez, Justus Just, Manuela Klaus, Rakesh Agrawal, and Thomas Unold, Real-time observation of Cu<sub>2</sub>ZnSn(S,Se)<sub>4</sub> solar cell absorber layer formation from nanoparticle precursors, *Phys. Chem. Chem. Phys.* **15**, 18281 (2013).
- [25] José Márquez, Helena Stange, Charles J. Hages, Norbert Schaefer, Sergiu Levenco, Sergio Giraldo, Edgardo Saucedo, Klaus Schwarzborg, Daniel Abou-Ras, Alex Redinger, Manuela Klaus, Christoph Genzel, Thomas Unold, and Roland Mainz, Chemistry and dynamics of ge in kesterite: Toward band-gap-Graded absorbers, *Chem. Mater.* **29**, 9399 (2017).
- [26] Cheng Zhu *et al.*, Strain engineering in perovskite solar cells and its impacts on carrier dynamics, *Nat. Commun.* **10**, 815 (2019).
- [27] Qingdong Ou, Xiaozhi Bao, Yinan Zhang, Huaiyu Shao, Guichuan Xing, Xiangping Li, Liyang Shao, and Qiaoliang Bao, Band structure engineering in metal halide perovskite nanostructures for optoelectronic applications, *Nano Mater. Sci.* **1**, 268 (2019).
- [28] Milton Ohring, *The Materials Science of Thin Films* (Academic Press, San Diego, 2001), 2nd ed., p. 794.
- [29] G. G. Stoney and Charles Algernon Parsons, The tension of metallic films deposited by electrolysis, *Proc. R. Soc. London. Ser. A, Containing Papers Math. Phys. Charact.* **82**, 172 (1908).
- [30] G. C. A. M. Janssen, Stress and strain in polycrystalline thin films, *Thin Solid Films* **515**, 6654 (2007).
- [31] D. Ngo, X. Feng, Y. Huang, A. J. Rosakis, and M. A. Brown, Thin film/substrate systems featuring arbitrary film thickness and misfit strain distributions. Part I: Analysis for obtaining film stress from non-local curvature information, *Int. J. Solids Struct.* **44**, 1745 (2007).
- [32] X. Feng, Y. Huang, and A. J. Rosakis, Multi-layer thin films/substrate system subjected to non-uniform misfit strains, *Int. J. Solids Struct.* **45**, 3688 (2008).
- [33] Y. Huang and A. J. Rosakis, Extension of Stoney's formula to non-uniform temperature distributions in thin film/substrate systems. The case of radial symmetry, *J. Mech. Phys. Solids* **53**, 2483 (2005).
- [34] M. A. Brown, A. J. Rosakis, X. Feng, Y. Huang, and Ersan Üstündag, Thin film/substrate systems featuring arbitrary film thickness and misfit strain distributions. Part II: Experimental validation of the non-local stress/curvature relations, *Int. J. Solids Struct.* **44**, 1755 (2007).
- [35] J. B. Landau, L. D. Lifshitz, and E. M. Sykes, *Theory of Elasticity* (Pergamon Press, Oxford, 1989).
- [36] J. R. Manning, *Diffusion Kinetics for Atoms in Crystals* (Van Nostrand, New York, 1968).
- [37] O. Lundberg, J. Lu, A. Rockett, M. Edoff, and L. Stolt, Diffusion of indium and gallium in Cu(In,Ga)Se<sub>2</sub> thin film solar cells, *J. Phys. Chem. Solids* **64**, 1499 (2003).
- [38] Dmytro Gavryushenko, Calculation of the diffusion flux in a binary solution in the case of a concentration-dependent

- diffusion coefficient, *Russ. J. Phys. Chem. A* **78**, 1584 (2004).
- [39] P. W. Voorhees and William C. Johnson, The thermodynamics of elastically stressed crystals, *Solid State Phys.* **59**, 1 (2004).
- [40] P. Mazur, Onsager's reciprocal relations and thermodynamics of irreversible processes, *Periodica Polytech. Chem. Eng.* **41**, 197 (1996).
- [41] Wai Cai and William D. Nix, *Imperfections in Crystalline Solids* (Press, Cambridge University, 2016).
- [42] E. Korhonen, K. Kuitunen, F. Tuomisto, A. Urbaniak, M. Igalson, J. Larsen, L. Gütay, S. Siebentritt, and Y. Tamm, Vacancy defects in epitaxial thin film CuGaSe<sub>2</sub> and CuInSe<sub>2</sub>, *Phys. Rev. B - Condens. Matter Mater. Phys.* **86**, 064102 (2012).
- [43] J. Srour, M. Badawi, F. El Haj Hassan, and A. V. Postnikov, Crystal structure and energy bands of (Ga/In)Se and Cu(In, Ga)Se<sub>2</sub> semiconductors in comparison, *Phys. Status Solidi (B) Basic Res.* **253**, 1472 (2016).
- [44] H. W. Spiess, U. Haebleren, G. Brandt, A. Rüber, and J. Schneider, Nuclear magnetic resonance in IB–III–VI<sub>2</sub> semiconductors, *Phys. Status Solidi (B)* **62**, 183 (1974).
- [45] Yi Cheng Lin, Xiang Yu Peng, Li Ching Wang, Yao Leng Lin, Cheng Han Wu, and Shih Chang Liang, Residual stress in CIGS thin film solar cells on polyimide: Simulation and experiments, *J. Mater. Sci.: Mater. Electron.* **25**, 461 (2014).
- [46] W. Paszkowicz, R. Minikayev, P. Piszora, D. Trots, M. Knapp, T. Wojciechowski, and R. Bacewicz, Thermal expansion of CuInSe<sub>2</sub> in the 11–1, 073 K range: An X-ray diffraction study, *Appl. Phys. A: Mater. Sci. Process.* **116**, 767 (2014).
- [47] H. G. Brühl and H. Neumann, Thermal expansion of CuGaSe<sub>2</sub>, *Solid State Commun.* **34**, 225 (1980).
- [48] H. T. Xue, W. J. Lu, F. L. Tang, X. K. Li, Y. Zhang, and Y. D. Feng, Phase diagram of the CuInSe<sub>2</sub>-CuGaSe<sub>2</sub> pseudobinary system studied by combined *Ab initio* density functional theory and thermodynamic calculation, *J. Appl. Phys.* **116**, 053512 (2014).
- [49] B. Namnuan, K. Yoodee, and S. Chatraphorn, Probing diffusion of In and Ga in CuInSe<sub>2</sub>/CuGaSe<sub>2</sub> bilayer thin films by x-ray diffraction, *J. Cryst. Growth* **432**, 24 (2015).
- [50] David J. Schroeder, Gene D. Berry, and Angus A. Rockett, Gallium diffusion and diffusivity in CuInSe<sub>2</sub> epitaxial layers, *Appl. Phys. Lett.* **69**, 4068 (1996).
- [51] Shi Luo, Jiun Haw Lee, Chee Wee Liu, Jia Min Shieh, Chang Hong Shen, Tsung Ta Wu, Dongchan Jang, and Julia R. Greer, Strength, stiffness, and microstructure of Cu(In, Ga)Se<sub>2</sub> thin films deposited via sputtering and co-evaporation, *Appl. Phys. Lett.* **105**, 011907 (2014).
- [52] Arnaud Gerthoffer, Frédéric Roux, Fabrice Emieux, Pascal Faucherand, Hélène Fournier, Louis Grenet, and Simon Perraud, CIGS solar cells on flexible ultra-thin glass substrates: Characterization and bending test, *Thin Solid Films* **592**, 99 (2015).
- [53] Arnaud Gerthoffer, Christophe Poulain, Frédéric Roux, Fabrice Emieux, Louis Grenet, and Simon Perraud, CIGS solar cells on ultra-thin glass substrates: Determination of mechanical properties by nanoindentation and application to bending-induced strain calculation, *Solar Energy Mater. Solar Cells* **166**, 254 (2017).
- [54] René Fouret, Bernard Hennion, J. Gonzalez, and S. M. Wasim, Elastic stiffness constants of copper indium diselenide determined by neutron scattering, *Phys. Rev. B* **47**, 8269 (1993).
- [55] Prayoosak Pluengphon and Thiti Bovornratanaraks, Phase stability and elastic properties of CuGaSe<sub>2</sub> under high pressure, *Solid State Commun.* **218**, 1 (2015).
- [56] A. S. Verma, Sheetal Sharma, R. Bhandari, B. K. Sarkar, and V. K. Jindal, Elastic properties of chalcopyrite structured solids, *Mater. Chem. Phys.* **132**, 416 (2012).
- [57] Ch Genzel, I. A. Denks, R. Coelho, D. Thomas, R. Mainz, D. Apel, and M. Klaus, Exploiting the features of energy-dispersive synchrotron diffraction for advanced residual stress and texture analysis, *J. Strain Anal. Eng. Des.* **46**, 615 (2011).
- [58] Jan Peter Bäcker, Sebastian S. Schmidt, Humberto Rodriguez-Alvarez, Christian Wolf, Christian A. Kaufmann, Manuel Hartig, Roland Mainz, and Rutger Schlattmann, Lateral phase separation in Cu-In-Ga precursor and, *Solar Energy Mater. Solar Cells* **162**, 120 (2017).
- [59] R. Mainz, A. Singh, S. Levchenko, M. Klaus, C. Genzel, K. M. Ryan, and T. Unold, Phase-transition-driven growth of compound semiconductor crystals from ordered metastable nanorods, *Nat. Commun.* **5**, 3133 (2014).
- [60] Sergio Ledesma, Gabriel Aviña, and Raul Sanchez, in *Simulated Annealing*, edited by Cher Ming Tan (IntechOpen, Rijeka, Croatia, 2008), Chap. 20.
- [61] H. Rodriguez-Alvarez, R. Mainz, R. Caballero, D. Abou-Ras, M. Klaus, S. Gledhill, A. Weber, C. A. Kaufmann, and H. W. Schock, Real-time study of Ga diffusion processes during the formation of Cu(In, Ga)Se<sub>2</sub>: The role of Cu and Na content, *Solar Energy Mater. Solar Cells* **116**, 102 (2013).
- [62] Chunjie Wang, Xue Li, and Yue Wang, First-principles calculations on electronic and elastic properties of CuInS<sub>2</sub> and CuInSe<sub>2</sub> at ambient pressure, *Adv. Intell. Syst. Res.* **156**, 176 (2017).
- [63] Fred Kocks, Carlos Tomé, and H.-R. Wenk, *Texture and Anisotropy. Preferred Orientations in Polycrystals and Their Effect on Material Properties* (Cambridge University Press, Cambridge, 2000).
- [64] Celeste A. M. van den Bosch, Andrea Cavallaro, Roberto Moreno, Giannantonio Cibin, Gwilherm Kerherve, José M. Caicedo, Thomas K. Lippert, Max Doebeli, José Santiso, Stephen J. Skinner, and Ainara Aguadero, Revealing strain effects on the chemical composition of perovskite oxide thin films surface, bulk, and interfaces, *Adv. Mater. Interfaces* **7**, 1901440 (2019).
- [65] Kyung Taek Cho, Sanghyun Paek, Giulia Grancini, Cristina Roldán-Carmona, Peng Gao, Yonghui Lee, and Mohammad Khaja Nazeeruddin, Highly efficient perovskite solar cells with a compositionally engineered perovskite/hole transporting material interface, *Energy Environ. Sci.* **10**, 621 (2017).
- [66] Nils Ross, Sigbjorn Grini, Katharina Rudisch, Lasse Vines, and Charlotte Platzer-Bjorkman, Selenium inclusion in Cu<sub>2</sub>ZnSn(S, Se)<sub>4</sub> solar cell absorber precursors



- for optimized grain growth, *IEEE J. Photovolt.* **8**, 1132 (2018).
- [67] R. A. Wibowo, H. Yoo, A. Hölzing, R. Lechner, S. Jost, J. Palm, M. Gowtham, B. Louis, and R. Hock, A study of kesterite  $\text{Cu}_2\text{ZnSn}(\text{Se}, \text{S})_4$  formation from sputtered Cu-Zn-Sn metal precursors by rapid thermal processing sulfoselenization of the metal thin films, *Thin Solid Films* **535**, 57 (2013).
- [68] Nils Ross, Sigbjorn Grini, Katharina Rudisch, Lasse Vines, and Charlotte Platzer-Bjorkman, Selenium inclusion in  $\text{Cu}_2\text{ZnSn}(\text{S}, \text{Se})_4$  solar cell absorber precursors for optimized grain growth, *IEEE J. Photovolt.* **8**, 1132 (2018).
- [69] B. E. Warren, *X-ray Diffraction*, Addison-Wesley Series in Metallurgy and Materials Engineering (Dover Publications, New York, 1990).